Journal of Power Sources 195 (2010) 5651–5659

Contents lists available at ScienceDirect

Journal of Power Sources

journal homepage: www.elsevier.com/locate/jpowsour

Effect of fluoride ions on corrosion behavior of SS316L in simulated proton exchange membrane fuel cell (PEMFC) cathode environments

Ying Yang [a], Lie-jin Guo [a], Hongtan Liu [a,b,*]

[a] State Key Laboratory of Multiphase Flow in Power Engineering, Xi'an Jiaotong University, Xi'an, Shaanxi 710049, PR China
[b] Department of Mechanical and Aerospace Engineering, University of Miami, Coral Gables, FL 33124, USA

ARTICLE INFO

Article history:
Received 18 March 2010
Accepted 19 March 2010
Available online 25 March 2010

Keywords:
Bipolar plate
Corrosion
Stainless steel
Proton exchange membrane fuel cell (PEMFC)
Passive film

ABSTRACT

In order to determine the suitability of SS316L as a bipolar plate material in proton exchange membrane fuel cells (PEMFCs), its corrosion behavior is studied under different simulated PEMFC cathode corrosion conditions. Solutions of 1×10^{-5} M H_2SO_4 with a wide range of different F^- concentrations at 70 °C bubbled with air are used to simulate the PEMFC cathode environment. Electrochemical methods, both potentiodynamic and potentiostatic, are employed to study the corrosion behavior. Scanning electron microscopy (SEM) is used to examine the surface morphology of the specimen after it is potentiostatic polarized under simulated PEMFC cathode environments. Auger electron spectroscopy (AES) analysis is used to identify the composition and the depth profile of the passive film formed on the SS316L surface after it is polarized in simulated PEMFC cathode environments. Photo-electrochemical (PEC) method and capacitance measurements are used to characterize the semiconductor passive films. The results of both the potentiodynamic and potentiostatic analyses show that corrosion currents increase with F^- concentrations. SEM examination results indicate that pitting occurs under all the conditions studied and pitting is more severe with higher F^- concentrations. From the results of AES analysis, PEC analysis and the capacitance measurements, it is determined that the passive film formed on SS316L is a bi-layer semiconductor, similar to a p–n heterojunction consisting of an external n-type iron oxide rich semiconductor layer (electrolyte side) and an internal p-type iron–chromium oxide semiconductor layer (metal side). Further analyses of the experimental results reveal the electronic structure of the passive film and shed light on the corrosion mechanisms of SS316L in the PEMFC cathode environment.

1. Introduction

Various materials for bipolar plates in proton exchange membrane fuel cells (PEMFCs) have been investigated in recent years. Initially bipolar plates are mainly made of graphite plates due to their low weight, good electrical conductivity and good chemical compatibility. However, graphite plates have many setbacks such as their brittleness, porous structure and high cost of manufacturing. Metals such as stainless steel are considered promising candidates for bipolar plate materials because of their high electrical conductivity, good mechanical strength and low manufacturing cost. Many studies showed that stainless steels are promising bipolar plate materials for commercial applications of PEMFC [1–4]. Austenite stainless steels, such as uncoated and surface treated SS316 and SS316L, have been studied as bipolar plate materials for PEMFC.

Wang and Northwood [1] studied the corrosion behavior of SS316L in simulated PEMFC cathode environment (0.5 M H_2SO_4 @ 70 °C). They found that it was easier to passivate SS316L in an O_2-containing environment leading to less corrosion of SS316L in the cathode environment. Wang et al. [2] studied the corrosion characteristics of stainless steels including SS316L in simulated PEMFC cathode environment (1 M H_2SO_4 + 2 ppm F^- @ 70 °C) and suggested that SS316L was not very suitable for bipolar plates for PEMFCs. Lafront et al. [3] studied the corrosion behavior of SS316L as a bipolar plate material in a simulated PEMFC cathode environment (12.5 ppm H_2SO_4 + 1.8 ppm HF (pH 3.2) @ 25 and 80 °C) by electrochemical noise technique and found that passive state was observed for SS316L in the simulated cathode environment.

Some researchers have provided experimental results in a more realistic PEMFC working environment [4,5]. Borup and Vanderborgh [5] suggested that the PEMFC operating conditions as pH 3.60 with F^- concentration of 1.8 ppm at anode and pH 4.02 with F^- concentration of 1.1 ppm at cathode. Agneaux et al. [4] analyzed working solutions from different PEMFC anode and cathode after

* Corresponding author at: Xi'an Jiaotong University, Xi'an, Shaanxi 710049, PR China; University of Miami, PO Box 248294, Coral Gables, FL 33124, USA.
Tel.: +86 29 8266 5591; +1 305 284 2019; fax: +1 305 284 2580.
E-mail addresses: hongtanliu@mail.xjtu.edu.cn, hliu@miami.edu (H. Liu).

0378-7753/$ – see front matter © 2010 Elsevier B.V. All rights reserved.
doi:10.1016/j.jpowsour.2010.03.064

Table 1
Main chemical composition of SS316L (wt.%).

Fe	Cr	Ni	Mo	Si	Cu	Other
69.3	16.9	10.5	2.23	0.516	0.506	Balance

500 h operation. They pointed out the anode solutions were more lightly loaded with ions than the cathode solutions, considering the overall contents of all elements. The F^- concentration is highest and less than 10^{-3} M at both the anode and cathode, and the other anions concentration were all less than 10^{-5} M with pH 5.7–6.3 at the anode and pH 4.9–6.3 at the cathode.

The F^- concentration in PEMFC environment is important due to two main reasons [5]: the amount of F^- in solution indicates degradation rates of the membrane and is an indication of the expected life span of the membrane, and F^- help to induce corrosion of bipolar plate materials as do other halide ions such as Cl^- and Br^-.

As can be seen from the above, even for the same material applied for PEMFC bipolar plates, different researchers obtained significantly different results. One of the main reasons is that different simulated PEMFC corrosion environments were chosen. First of all, the pH values chosen by different researchers were different. Besides, some researchers added fluoride ions into corrosion solutions but some did not. Furthermore, the concentrations of F^- ions varied widely among different researchers. Such variations are reasonable since different fuel cells are often operated under different conditions, thus the degradation rates of the membrane must be different, which leads to different concentrations of F^- ions. Besides, the flow fields and structures of bipolar plates are different, so F^- concentrations must be different at different locations. Considering the above, it is very important to study the corrosion behaviors of bipolar plate materials in PEMFC environments containing different F^- concentrations. In this study, a solution of 1×10^{-5} M H_2SO_4 was chosen as the basic solution and different concentrations of F^- (NaF as the source of the F^-) were used to simulate different PEMFC environments. Since SS316L is probably the most promising candidate for metallic bipolar plates it is chosen in this work. Corrosion behavior of SS316L is evaluated with electrochemical and photo-electrochemical methods to reveal the corrosion mechanism of SS316L in the PEMFC cathode environment. Scanning electron microscope (SEM) and Auger electron spectroscopy (AES) are employed to character the surface topography and composition of the passive film after SS316L is polarized in different simulated PEMFC cathode environments.

2. Experimental systems and methodologies

2.1. Material and simulated solutions

2.1.1. Material

The main chemical composition of SS316L is shown in Table 1.

SS316L specimens were machined into cylinders with a diameter of 10 mm and a length of 7 mm. One end and the side of the specimens were sealed by silicone and polyethylene heat-shrink tubing, leaving only one end exposed. The sealed end of the specimen was connected with a copper wire and the exposed end was used as the working surface for electrochemical and photo-electrochemical measurement. The working surface was polished with 800-grit silicon carbide abrasive paper, rinsed with acetone and de-ionized water, and dried in nitrogen gas.

2.1.2. Simulated solutions

In this study, a solution of 1×10^{-5} M H_2SO_4 with different concentrations of F^- (0, 3×10^{-4}, 6×10^{-4}, 1×10^{-3} and 5×10^{-3} M) was used to examine the effect of F^- concentration on the corrosion behavior of SS316L under the PEMFC cathode condition. For each concentration, 1000 mL simulated solution was transferred to the corrosion cell. Pre-bubbling was carried out 1 h before each measurement and the solution was bubbled with air during measurement.

2.2. Electrochemistry analyses

The electrochemical experiments were carried out in a corrosion cell consisting of a three-electrode arrangement with one gas inlet tube and one gas outlet tube. The specimen served as the working electrode and a platinum sheet as the counter electrode. A saturated calomel electrode (SCE) connected to a salt-bridge probe with a Vycor frit tip served as the reference electrode, and the probe tip could be easily adjusted to be very close to the working electrode surface. In this study, potentials were measured against this SCE without correction for the thermal junction potential. All the potentials are referenced to the SCE except stated otherwise.

The corrosion cell was immersed in a temperature controlled water bath and the solution was kept at 70 °C and was bubbled thoroughly with pressurized air prior to and during the electrochemical measurements. The tests were conducted using a PAR 273A potentiostat (EG&G) coupled with a 5210 lock-in Amplifier (Signal recovery). The PowerSuite software was used for the electrochemical data acquisition and processing. Each experiment was repeated by using different specimens to ensure reproducibility of the results.

2.2.1. Potentiodynamic and potentiostatic measurements

At the beginning of each potentiodynamic experiment, the specimen was polarized cathodically for 10 min to remove oxides on the specimen surface and then stabilized at open circuit potential (OCP) for 1 h. Then the potentiodynamic test was carried out. In potentiodynamic tests, specimens were polarized at a scanning rate of 1 mV s^{-1} in a potential range from −0.2 V vs. OCP to 1.2 V. In potentiostatic tests, specimens were held at a potential of 0.6 V to simulate the PEMFC cathode condition. After polarizied cathodically for 10 min, the specimen was then potentiostatic polarized for 5 h.

2.2.2. Capacitance measurement

In this measurement, potential sweeps were carried out from anodic potential of 0.4 V to cathodic potential of −0.3 V at a scan rate of 25 mV per step. The data acquisition frequency of 188 Hz is chosen in the flat region of capacitance vs. frequency plots, so that the influence of acquisition frequency to capacitance measurement can be minimized.

2.3. Photo-electrochemistry

Photo-electrochemical (PEC) experiments were carried out in a PEC cell equipped with a flat quartz optical window. The test cell was kept at 70 °C with a water jacket and was bubbled thoroughly with pressurized air prior to and during the PEC measurements. PEC measurements also used three-electrode arrangement. The specimen polarized at 0.6 V for 5 h in a solution of 1×10^{-5} M H_2SO_4 with different concentrations of F^- served as the working electrode, a platinum sheet as the counter electrode and a SCE as the reference electrode. The PEC experiments are performed in the same solutions.

The photocurrents were generated by illuminating the entire working electrode surface by a 500 W Xenon lamp and a 1200/mm grating monochromator. A PAR 273A potentiostat (EG&G) coupled with a 5210 lock-in Amplifier (Signal recovery) and a light chopper (PAR 197, EG&G, f = 17.3 Hz) were used to measure the photocurrent, and the PEC system was controlled by a software developed

in-house. The photocurrent spectra were obtained on specimens polarized at 0.6 V by scanning the wavelength of light in steps of 10 nm from 320 nm to 650 nm. The photocurrent was corrected for the output of the lamp and the efficiency of the monochromator by using a calibrated photodiode. Calibrations were performed before and after each set of experiment.

2.4. Scanning electron microscope

In order to observe the surface topography changes of the specimens that were potentiostatic polarized at 0.6 V for 5 h in 1×10^{-5} M H_2SO_4 solutions with different F^- concentrations (0, 3×10^{-4}, 6×10^{-4}, 1×10^{-3} and 5×10^{-3} M), the samples were characterized using a JSM-6390A scanning electron microscope (SEM).

2.5. Auger electron spectroscopy

Auger electron spectroscopy (AES) was taken after each specimen was potentiostatic polarized at 0.6 V for 5 h in 1×10^{-5} M H_2SO_4 solutions with different F^- concentrations (0, 3×10^{-4}, 6×10^{-4}, 1×10^{-3} and 5×10^{-3} M). AES was used to analyse the composition profiles of elements Fe, Ni, Cr and O in the passive film, and was carried out with a PHI595 scanning Auger microscopy. The chamber base pressure was 5×10^{10} Torr (6.666×10^{12} Pa). Sputtering was performed at a pressure of about 5×10^{7} Torr (6.666×10^{9} Pa) with a 4.5 keV argon ions beam, while the sputtered area was 2 mm × 2 mm. The sputtering rate was around 40 nm min^{-1}.

3. Results and discussion

3.1. Potentiodynamic study

It is well known that the PEMFC cathode environment is aerobic. In such an acid environment, the metal corrosion process is an electrochemical process which involves both oxidation and reduction reactions [6]. The oxidation reactions can be represented as:

$$M \rightarrow M^{n+} + ne^- \quad (1)$$

where M represents surface metal elements, M^{n+} the corresponding metal ions in the solution and e^- free electrons.

The reduction reaction can be represented as:

$$O_2 + 4H^+ + 4e^- \rightarrow 2H_2O \quad (2)$$

where O_2 represents dissolved oxygen and H^+ proton adsorbed on the metal surface.

After the specimen was immersed in the corrosion solution, the equilibrium potential (corrosion potential, E_{corr}) and the associated current density (corrosion current, i_{corr}) can be measured by an electrochemical polarization method [7]. The corrosion potential and corrosion current density are widely used as indicators of the material corrosion resistance. A high corrosion potential and a low corrosion current density indicate that the corrosion of material is retarded.

Material corrosion resistance can be characterized by means of measuring the polarization resistance [7]. The polarization resistance is determined by extrapolating the tangential line of the polarization curve and it is given by,

$$R_p = \frac{\beta_a \beta_c}{2.3 i_{corr}(\beta_a + \beta_c)} \quad (3)$$

where R_p is the polarization resistance, i_{corr} the corrosion current density, β_a and β_c the Tafel slopes of the anodic and cathodic reactions, respectively.

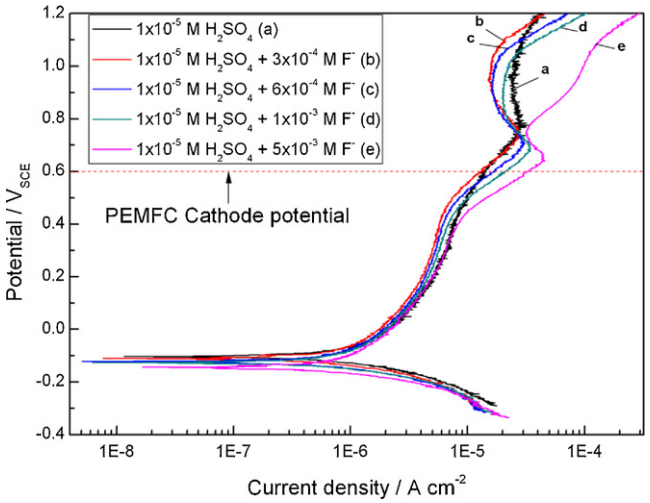

Fig. 1. Polarization curves for SS316L at 70 °C in 1×10^{-5} M H_2SO_4 solution with different concentrations of F^- (0, 3×10^{-4}, 6×10^{-4}, 1×10^{-3} and 5×10^{-3} M) bubbled with air.

Fig. 1 displays potentiodynamic polarization curves for SS316L at 70 °C in 1×10^{-5} M H_2SO_4 solution with different F^- concentrations bubbled with air. Table 2 shows the corresponding polarization parameters, which were obtained by fitting the polarization curves shown in Fig. 1 by using the PowerSuite software. The polarization curves show the self-passivation behavior for SS316L in all solutions [8]. From Fig. 1, it is clear that corrosion potential decreases and corrosion current increases, which means the corrosion resistance of SS316L decreases, with the increase of F^- concentration under the free corrosion condition. The corrosion current density of SS316L increases rapidly with increasing applied potential in the region from free corrosion potential to −0.05 V, due to the accelerated SS316L dissolution by anodic polarization. From −0.05 V to 0.2 V, the corrosion rates decrease gradually. From 0.2 V to around 0.5 V, every polarization curve changes from the active region to the passive region directly, which indicates the formation of a passive film on the surface of SS316L. The passive regions are narrow, which indicates that the passive capability of SS316L is low in the PEMFC cathode environment. At around 0.5 V, corrosion currents increase rapidly again, indicating that pitting takes place on the surface of SS316L. It is clear that the pitting potential decreases with increasing F^- concentration, indicating that it is easier for pitting to take place on SS316L in solutions with higher F^- concentrations. Besides, from this potential to around 0.8 V, there are peaks which could be attributed to transpassivation due to the formation of high valence chromium [9,10].

From Fig. 1 and Table 2, it can be seen that both the corrosion potential and corrosion current are highest in solution without F^-. These results indicate that when F^- concentration is low, it may have corrosion inhibiting effect for SS316L in 1×10^{-5} M H_2SO_4 solution under the free corrosion condition. When applied potential increases from 0.4 V to 0.65 V, the corrosion inhibiting role of F^- decreased gradually. It can be concluded that the corrosion potential and polarization resistance of SS316L decrease and the corrosion current of SS316L increase with increasing F^- concentration. These results show that the corrosion resistance of SS316L decreases with increasing F^- concentration when applied potential is between 0.4 V and 0.65 V.

At the cathode potential corresponding to a typical PEMFC's operating condition (0.6 V, the horizontal line marked in Fig. 1), the corresponding corrosion current densities of SS316L in different solutions are shown in Table 2. It can be seen that the corrosion current of SS316L at 0.6 V increases with increasing F^- concentra-

Table 2
Polarization parameters of SS316L at 70 °C in 1×10^{-5} M H_2SO_4 solution with different concentrations of F^- (0, 3×10^{-4}, 6×10^{-4}, 1×10^{-3} and 5×10^{-3} M) bubbled with air.

Concentration of F^- (M)	β_a (V)	β_c (V)	E_{corr} (V vs. SCE)	i_{corr} ($\mu A\,cm^{-2}$)	R_p ($\Omega\,cm^2$)	$I_{0.6\,V\,vs.\,SCE}$ ($\mu A\,cm^{-2}$)
Without F^-	0.200	0.094	−0.103	0.854	32592	14.1
3×10^{-4}	0.134	0.068	−0.110	0.498	39478	13.1
6×10^{-4}	0.142	0.070	−0.123	0.526	38747	16.8
1×10^{-3}	0.164	0.070	−0.126	0.621	34484	20.9
5×10^{-3}	0.212	0.072	−0.144	0.677	34323	32.8

tion, which means corrosion resistance of SS316L decreases with increasing F^- concentration at 0.6 V. It is noticed that the cathode potential corresponding to the typical PEMFC's operating condition lies in the transpassive region of polarization curves, which indicates the occurrence of pitting on the surface of SS316L under typical fuel cell operating conditions.

3.2. Potentiostatic sudies

To study the long-term corrosion behavior of SS316L in 1×10^{-5} M H_2SO_4 with different F^- concentrations bubbled with air, potentiostatic measurements were performed for 5 h and the results are shown in Fig. 2.

From Fig. 2, it can be seen that there was a fast decay for the current density of SS316L in every solution after it was applied with a constant potential of 0.6 V. The currents of SS316L in all solutions are stabilized after about 2000 s, indicating that a stable passive state was established. After 3000–4500 s, the corrosion current densities are lower than the US DOE 2015 target, 1 $\mu A\,cm^{-2}$ [11]. It can also be seen that the higher the F^- concentration is, the higher is the corrosion current density and the trend is similar to that found in the potentiodynamic studies. Besides, the time needed for the current density to decrease to 1 $\mu A\,cm^{-2}$ increases with F^- concentration. It can also be seen that the current density decreases continuously with continued potentiostatic polarization.

3.3. Surface morphology

The surface topography of SS316L after potentiostatic polarization at 0.6 V for 5 h in the simulated PEMFC cathode environments is examined by SEM and the results are shown in Fig. 3. It can be seen that pitting occurred on the surface of SS316L in every solution. Even though it is not clear from the limited areas of the SEM photos, this result together with the results of potentiodynamic studies indicate that pitting becomes more serious as F^- concentration increases.

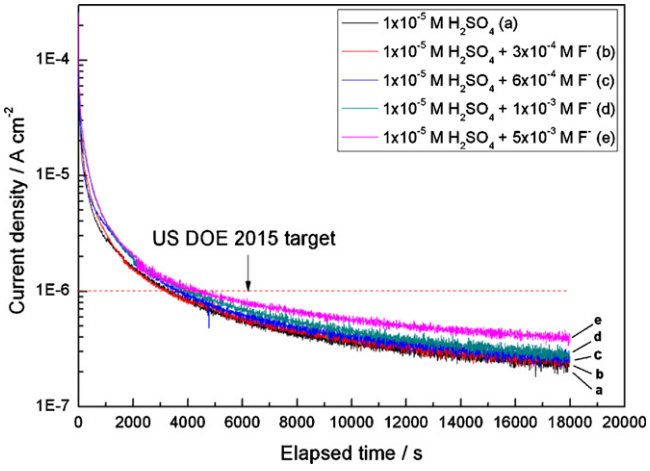

Fig. 2. Potentiostatic plots for SS316L at 70 °C in 1×10^{-5} M H_2SO_4 solution with different concentrations of F^- (0, 3×10^{-4}, 6×10^{-4}, 1×10^{-3} and 5×10^{-3} M) bubbled with air.

3.4. Auger electron spectroscopy analysis

The composition profiles of elements Fe, Cr, Ni and O in the passive films formed on SS316L polarized at 0.6 V for 5 h at 70 °C in 1×10^{-5} M H_2SO_4 solution with different concentrations of F^- bubbled with air were obtained by AES. The results are shown in Fig. 4. The depth profiles of Cr/Fe atomic ratio for the passive films are shown in Fig. 5.

Based on the content changes of elements Fe and Cr in Figs. 4 and 5, the thickness of the passive films, distance from the surface to the top of Cr/Fe peak [12], corresponding to F^- concentrations of 0, 3×10^{-4}, 6×10^{-4}, 1×10^{-3} and 5×10^{-3} M can be obtained as approximately 8 nm, 10 nm, 12 nm, 8 nm and 4 nm, respectively. It is noticed that the passive film thickness is not linearly correlated with F^- concentrations. The passive film thickness first increases and then deceases with F^- concentration, thus there exists a maximum thickness and it is formed when F^- concentration in solutions is about 6×10^{-4} M.

From Fig. 4a–d, it is found that the content change of Fe can be divided into two regions in the depth profile. In the first region, from 0 to about 4 nm, Fe content increases rapidly; while in the second region, from about 4 nm to about 8–12 nm, it changes slightly. In these two regions, Cr content decreases to a minimum in the first region and increases rapidly to a maximum in the second region. Ni content can be considered constant in the depth profile. From Fig. 5, it is clear that the Cr/Fe atomic ratio decreases rapidly in the first region and increases steeply in the second region. Based on the above observations, the passive film can be considered to be consisting of two layers, an iron oxide rich outer layer and an iron–chromium oxide inner layer.

From the AES analysis, it is noticed that Fe content is dominant in the passive film and should behave as an n-type semiconductor. More discussions on this will be provided later with the capacitance and photo-electrochemical measurement results.

3.5. Capacitance measurement

The charge distribution at the passive film–electrolyte interface is often determined by measuring the capacitance of the space charge layer C as a function of the electrode potential E. It assumed that the capacitance response is controlled by the band bending and can be described by the variation of the space charge capacitance under depletion conditions. In the case of a passive film–electrolyte interface, the potential dependence of the space charge layer is described by the Mott–Schottky equation [13]:

$$\frac{1}{C^2} = \frac{2}{eN_D\varepsilon\varepsilon_0}\left(E - E_{fb} - \frac{kT}{e}\right) \quad (4)$$

for an n-type semiconductor and

$$\frac{1}{C^2} = \frac{2}{-eN_A\varepsilon\varepsilon_0}\left(E - E_{fb} - \frac{kT}{e}\right) \quad (5)$$

for a p-type semiconductor, where ε is the dielectric constant of the film, taken as 15.6 [14]; ε_0 the permittivity of free space (8.85×10^{-12} F m^{-1}); e the electron charge; N_D and N_A the donor

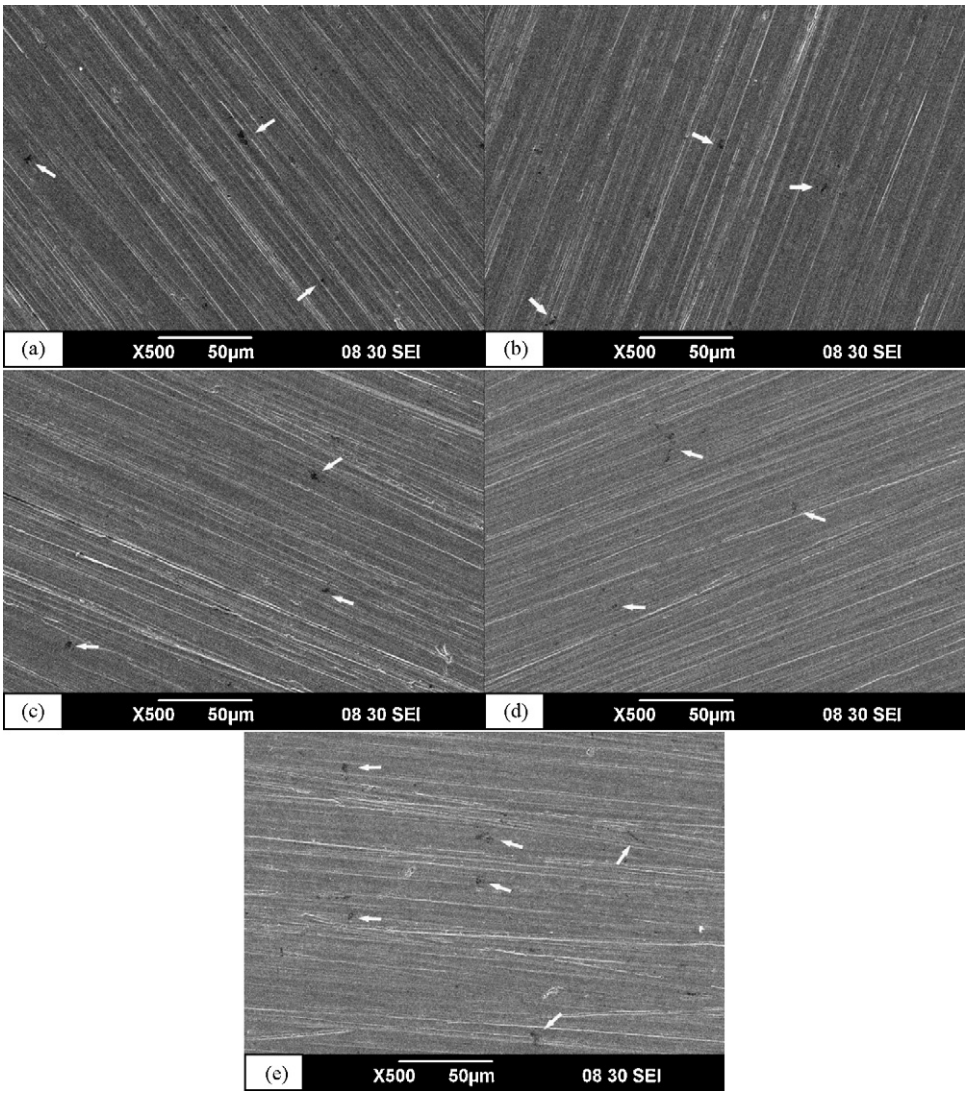

Fig. 3. SEM micrographs of SS316L polarized at 0.6 V for 5 h at 70 °C in 1×10^{-5} M H_2SO_4 solution with different F^- concentrations bubbled with air. (a) Without F^-, (b) 3×10^{-4} M F^-, (c) 6×10^{-4} M F^-, (d) 1×10^{-3} M F^-, and (e) 5×10^{-3} M F^-. Arrows point out some pitting.

and acceptor densities, respectively; E_{fb} the flat band potential; k the Boltzmann's constant; and T the absolute temperature.

The validity of the Mott–Schottky analysis is based on the assumption that the capacitance of the Helmholtz layer is much greater than that of the space charge layer [15]. When the measured frequency is high, the contribution of the Helmholtz capacitance to the measured electrode capacitance can be neglected. In this case the capacitance of the passive film–electrolyte interface expresses the capacitance of the space charge layer of the passive film, so E_{fb} can be extrapolated from $C^{-2} = 0$, while N_D and N_A can be determined from the slope of the experimental C^{-2} vs. E plots.

Fig. 6 shows Mott–Schottky plots for passive films formed on SS316L at 70 °C in 1×10^{-5} M H_2SO_4 solutions with different concentrations of F^- bubbled with air. From Fig. 6, it is noticed that the capacitance increases with increasing F^- concentration in solution. For each case, when the applied potential decreases from 0.1 V to −0.25 V, the capacitance of the passive film first increases rapidly, reaching a maximum and then decreases. The increase of capacitance is due to the decrease of the thickness of the electron depletion layer and (the decrease of) accumulating number of charge carriers, the decrease of capacitance is attributed to the decrease of hole concentration in the valence band [12,14]. From Fig. 6, it can be seen that Mott–Schottky plots reveal duplex character of the passive films with an n-type semiconductor behavior (positive slope, from around 0.1 V to around −0.1 V) and a p-type semiconductor behavior (negative slope, from around −0.15 V to around −0.25 V), even though the p-type semiconductor behavior is not as pronounced. This result confirms the finding from the AES analysis, from which it is found that the passive film consists two layers and behaves more as an n-type semiconductor. The duplex character of the passive film formed on stainless steel was also observed by other researchers in other corrosion environments [12,16,17].

The flat band potential is chosen from the bottom of the valley on C^{-2} vs. E plots (the turning point of n-type behavior to p-type behavior) [18]. The passive film behaves as an n-type semiconductor when the applied potential is higher than the flat band potential and a p-type semiconductor when the applied potential is lower than the flat band potential. The value of the flat band potential for SS316L in different solutions is shown in Table 3. It can be observed that the flat band potential for SS316L decreases with the increase of F^- concentration.

The value of the donor densities of the n-type semiconductor and acceptor densities of the p-type semiconductor of passive films formed on SS316L in different solution are determined by Eqs. (4)

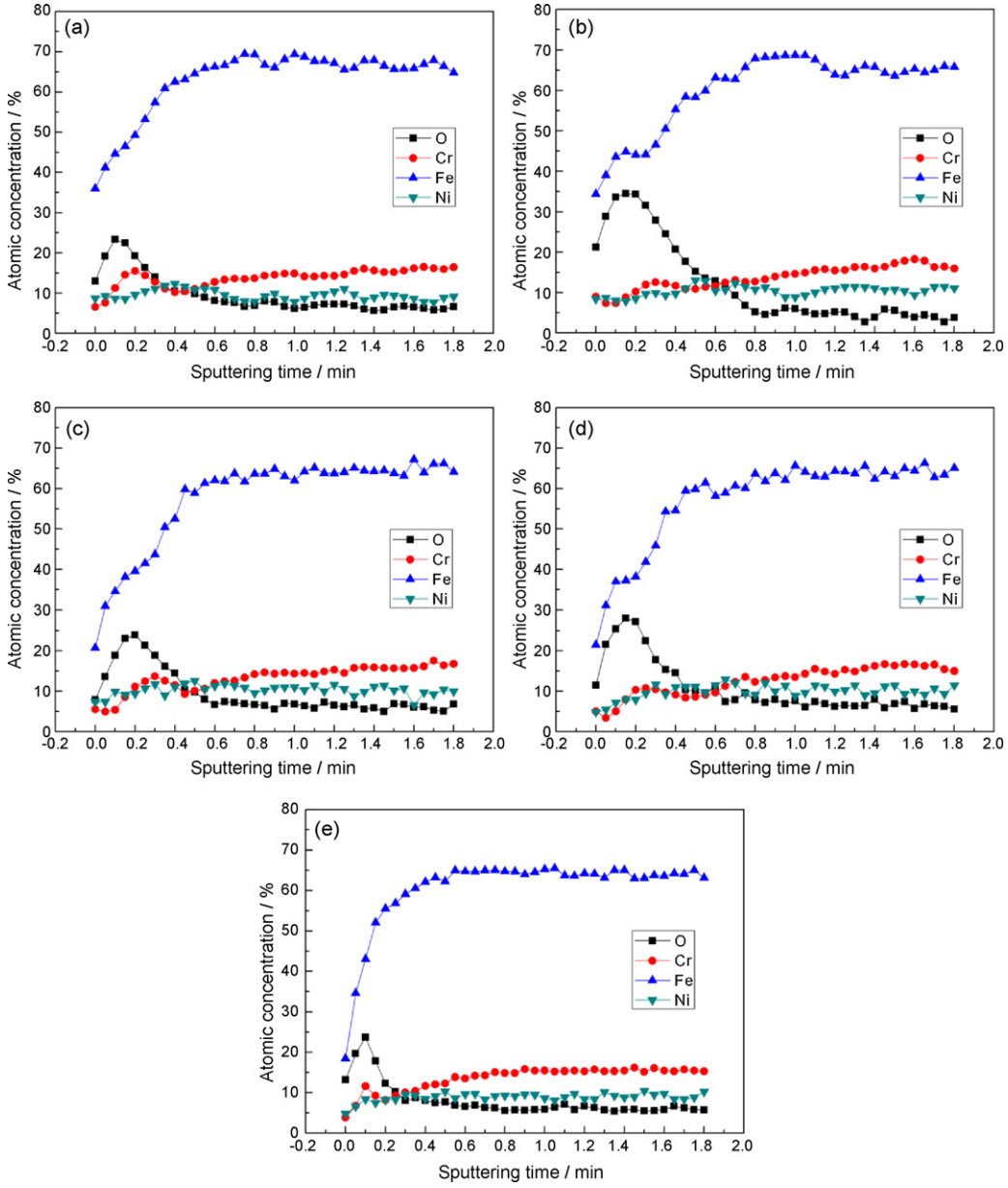

Fig. 4. AES depth profiles of passive films formed on SS316L polarized at 0.6 V for 5 h at 70 °C in 1×10^{-5} M H_2SO_4 solution with different F^- concentrations bubbled with air. (a) Without F^-, (b) 3×10^{-4} M F^-, (c) 6×10^{-4} M F^-, (d) 1×10^{-3} M F^-, and (e) 5×10^{-3} M F^-.

and (5) and shown in Table 3. It is found that the acceptor density is higher than the donor density for every passive film formed on SS316L in each of the solutions.

From Table 3, it is clear that both donor densities and acceptor densities increase with the increase of F^- concentration. With increasing F^- concentration, the donor densities of passive films increase from 3.26×10^{20} cm^{-3} to 1.25×10^{21} cm^{-3}. For acceptor densities, it increases from 3.46×10^{20} cm^{-3} to 8.04×10^{21} cm^{-3}. The donor and acceptor densities represent the defects, oxygen vacancies or cation vacancies in the passive film. Since a greater number of defects generally indicate a lower corrosion resistance, this provides another explanation on why the corrosion resistance of SS316L decreases as the F^- concentration increases.

Table 3
Semiconductor parameters for capacitance measurement of SS316L polarized at 0.6 V for 5 h at 70 °C in 1×10^{-5} M H_2SO_4 solution with different concentrations of F^- (0, 3×10^{-4}, 6×10^{-4}, 1×10^{-3} and 5×10^{-3} M) bubbled with air.

Concentration of F^- (M)	E_{fb} (vs. SCE)	Carrier density (cm^{-3})	
		N_D	N_A
Without F^-	−0.125	2.52×10^{20}	6.45×10^{20}
3×10^{-4}	−0.125	3.26×10^{20}	3.46×10^{20}
6×10^{-4}	−0.150	4.19×10^{20}	7.61×10^{20}
1×10^{-3}	−0.150	6.18×10^{20}	1.31×10^{21}
5×10^{-3}	−0.200	1.25×10^{21}	8.04×10^{21}

3.6. Photo-electrochemical analyses

There is a simplified relationship between photocurrent and photon energy of the incident light for passive films, this relationship can be described by [19,20],

$$\frac{i_{ph} h\nu}{I} = \alpha(h\nu - E_g)^2 \quad (6)$$

where i_{ph} is the photocurrent, $h\nu$ the photon energy of the incident light, I the intensity of the incident light, α the optical absorp-

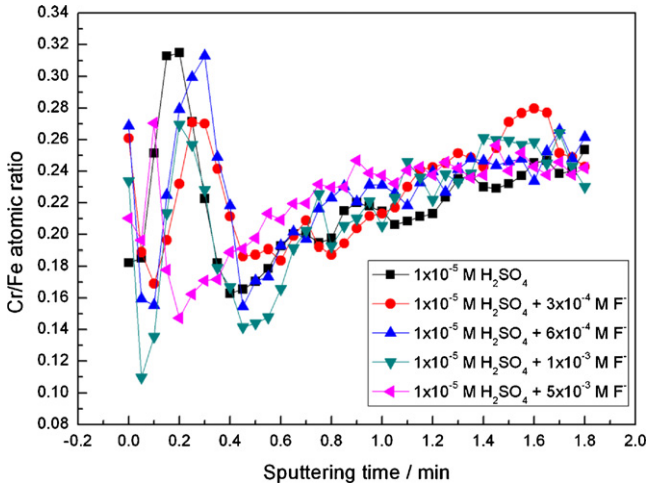

Fig. 5. Cr/Fe atomic ratio for the passive film formed on SS316L polarized at 0.6 V for 5 h at 70 °C in 1×10^{-5} M H_2SO_4 solution with different F^- concentrations bubbled with air. (a) Without F^-, (b) 3×10^{-4} M F^-, (c) 6×10^{-4} M F^-, (d) 1×10^{-3} M F^-, and (e) 5×10^{-3} M F^-.

tion coefficient and E_g the band gap energy. The band gap can be obtained by extrapolating the $(i_{ph}h\nu/I)^{0.5}$ plot from the photocurrent spectra, and the intercept of the straight line with the photon energy axis is the band gap of the semiconductor.

Fig. 7 shows the $(I_{ph}h\nu/I)^{0.5}$ vs. $h\nu$ plots and the band gap energy can be estimated as the photon energy at which $(i_{ph}h\nu/I)^{0.5}$ equals to zero. The band gap energies of the passive film with different F^- concentrations (0, 3×10^{-4}, 6×10^{-4}, 1×10^{-3} and 5×10^{-3} M) obtained from Fig. 7 are 2.46, 2.62, 2.80, 2.81 and 2.98 eV, respectively. It can be seen that the band gap becomes broader as F^- concentration increases. Besides, it is easier to generate photocurrent for passive films formed on SS316L with higher F^- concentration (inset in Fig. 7), which may be attributed to the varying electric field that promote the photogenerated charges separation and transport. This result indicates that a change in F^- concentration results in a change of the semiconductor structure of the passive film formed on SS316L. The potentiodynamic measurement results show 0.6 V lies in the transpassive region of polarization curves. In this transpassive region, chromium may change from a low valence to a high valence [9,10].

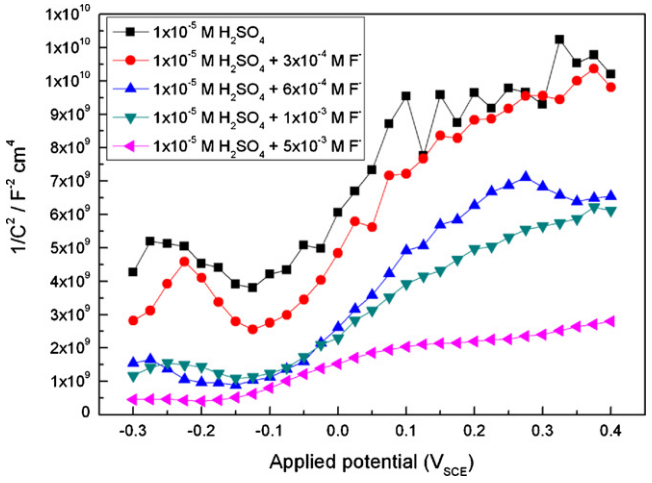

Fig. 6. Mott–Schottky plots for passive films formed on SS316L at 70 °C in 1×10^{-5} M H_2SO_4 solution with different concentrations of F^- (0, 3×10^{-4}, 6×10^{-4}, 1×10^{-3} and 5×10^{-3} M) bubbled with air.

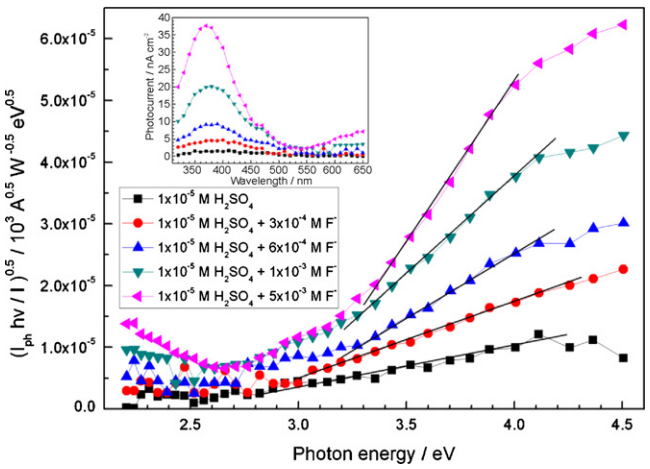

Fig. 7. $(I_{ph}h\nu/I)^{0.5}$ vs. $h\nu$ plots for SS316L at 70 °C potentiostatic polarized for 5 h in 1×10^{-5} M H_2SO_4 solution with different concentrations of F^- (0, 3×10^{-4}, 6×10^{-4}, 1×10^{-3} and 5×10^{-3} M) bubbled with air. Inset: Rough photocurrent spectrum.

The $(I_{ph}h\nu/I)^{0.5}$ vs. $h\nu$ plots show that photocurrents are positive during illumination, which shows that the semiconductor behavior of the passive film resembles more of an n-type semiconductor. This result confirms both the AES results and the capacitance analysis.

3.7. Electronic structure of passive films

As discussed above, the passive film formed on SS316L is similar to a p–n heterojunction constituted by an external n-type iron oxide rich semiconductor layer (electrolyte side) and an internal p-type iron–chromium oxide semiconductor layer (metal side). This kind of structure has been reported by other researchers [12,16–18,21], such as films formed on SS304 inside a furnace in atmosphere [12], films formed on SS316L in high temperature basic aqueous environments [16], films formed on Fe–Cr alloy in 0.1 M H_2SO_4 [17], films formed on SS304 in a borate buffer solution [18] and Cr-oxide films deposited on SS446 [21]. When an electrode is immersed in a redox electrolyte and under a free corrosion condition, the Fermi level of the semiconductor is controlled by the electrochemical potential of the redox system, so band bending takes place in the semiconductor. However, when the semiconductor was applied with potential, the Fermi level of the semiconductor is controlled by the applied potential.

The energy band model for SS316L in different corrosion solutions is shown in Fig. 8 for various applied potentials. The band energy change at the interface of between the passive film and the electrolyte will be discussed in detail below.

When the applied potential is higher than the flat band potential, the band of external semiconductor bends downward and the space charge layer at the passive film–electrolyte interface develops into a depleted region (Fig. 8a). Due to the downward bending, the inward migrations of electrons and anions and the outward migrations of the metal cations are facilitated at the passive film–electrolyte interface. Thus, the passive film tends to grow thicker, but at the same time, it is easier for the harmful anions such as SO_4^{2-} and F^- to penetrate the external n-type semiconductor film and result in localized corrosion. The harmful anions will encounter the Schottky barrier (p–n heterojunction) and it will hinder their further penetration into the p-type semiconductor film.

The capacitance analysis results show that the flat band potential of SS316L decreases with increasing F^- concentration, thus the band bending (passive film–electrolyte interface) increases when SS316L electrodes are applied with the same potential. Hence, the

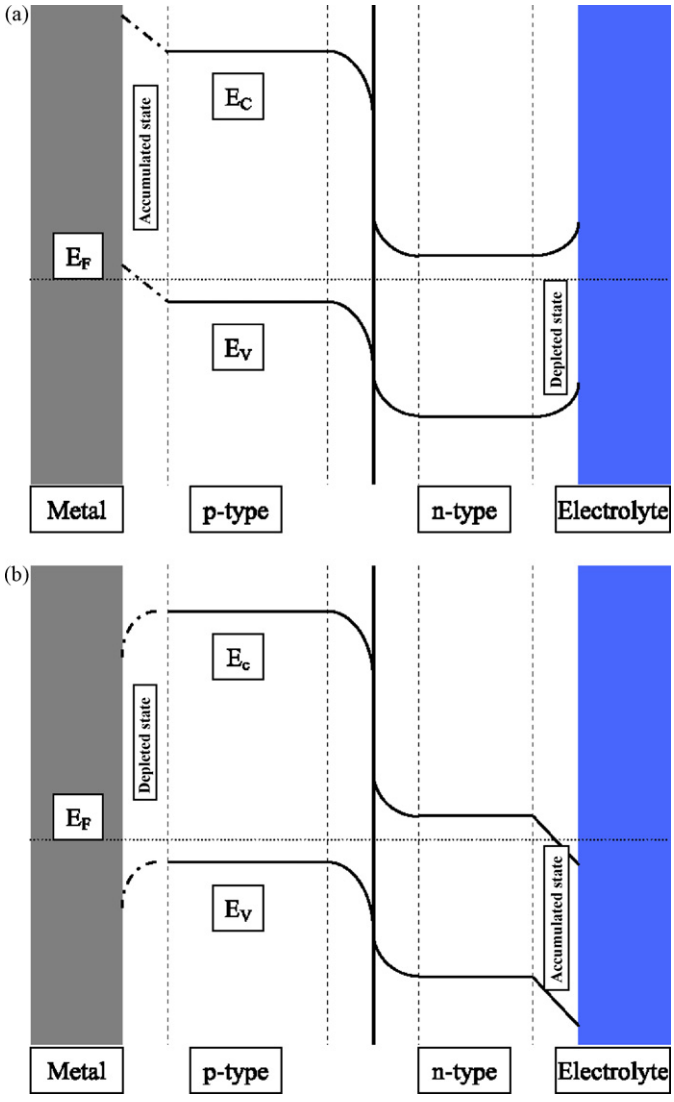

Fig. 8. Schematics of the band structure model of the different passive films formed on SS316L in simulated PEMFC cathode environment. E_F: Fermi level, E_C: edge of conduction band, and E_V: edge of valence band. (a) Applied potential greater than the flat band potential; (b) applied potential lower than the flat band potential.

pitting corrosion resistance of SS316L decreases with the increase of F^- concentration.

When the applied potential is lower than the flat band potential, the band of external semiconductor bends upward and the space charge layer at the passive film–electrolyte interface develops into an accumulated region (Fig. 8b), which forms an energy barrier against the outward migration of metal cations and hinder passive film growth. As a result, a passive film with this electronic structure is weak in protecting the substrate.

From the results discussed above, it can be concluded that when the flat band potential is lower, the corrosion resistance is higher due to the passive film growth enhancement, but at the same time it is easier for the aggressive anions such as SO_4^{2-} and F^- to penetrate the external n-type semiconductor film and result in localized corrosion. Based on these analysis and flat band potential results (Table 3), the local corrosion of SS316L is more severe in solution containing higher F^- concentration, consistent with the SEM results shown in Fig. 3.

The PEMFC's cathode working potential is higher than the flat band potential of SS316L in every corrosion solution presented in this paper, which means the films will protect the metal substrate; however they cannot completely prevent harmful ions to penetrate into the metal substrate, causing pitting corrosions.

4. Conclusions

The corrosion behavior of SS316L in simulated PEMFC cathode environments with different F^- concentrations are studied by electrochemical techniques, scanning electron microscopy (SEM), photo-electrochemical techniques and Auger electron spectroscopy (AES) analysis. It is found that SS316L under PEMFC cathode working conditions satisfies the US DOE's 2015 corrosion criterion, but pitting corrosion cannot be completed avoided. It is also found that the corrosion resistance of SS316L decreases with the increase of F^- concentration in the solution.

From the AES analysis and the capacitance measurement, it is found that the passive film is a p–n heterojunction semiconductor (bi-layer structure) with an external n-type iron oxide rich layer and an internal p-type iron–chromium oxide layer, and the n-type characteristic is more pronounced. The Mott–Schottky analysis provides an explanation on why the corrosion resistance of SS316L decreases as the F^- concentration increases. Further analysis by the photo-electrochemical technique confirms the bi-layer structure of the passive film and showed that the band gap becomes broader as F^- concentration increases, again confirming that the corrosion resistance decreases with the increase of F^- concentration.

Further analyses of the electronic structure of the passive films indicates that when the applied potential is at a PEMFC's typical cathode potential, the band of the external semiconductor bends downward and the space charge layer at the passive film–electrolyte interface develops into a depleted region. Such a structure forms an energy barrier for the outward migration of electrons while promotes metal ions migrating from substrate to the film, which facilitates the growth of passive film. However, this cannot completely prevent harmful ions from penetrating into the metal substrate.

Acknowledgements

The financial supports of Chang Jiang Scholars Program of Ministry of Education of China, the National Natural Science Foundation of China (No. 50521604) and National Basic Research Program of China (No. 2009CB220000) are gratefully acknowledged. Authors would also like to thank Ms. Guiyin Chen for her assistance in part of the electrochemical experiments, and Dr. Mingtao Li and Dr. Jinzhan Su for valuable discussions on photo-electrochemical techniques.

References

[1] Y. Wang, D.O. Northwood, Electrochim. Acta 52 (2007) 6793–6798.
[2] H. Wang, M.A. Sweikart, J.A. Turner, J. Power Sources 115 (2003) 243–251.
[3] A.M. Lafront, E. Ghali, A.T. Morales, Electrochim. Acta 52 (2007) 5076–5085.
[4] A. Agneaux, M.H. Plouzennec, L. Antoni, J. Granier, Fuel Cells 6 (2006) 47–53.
[5] R.L. Borup, N.E. Vanderborgh, Mater. Res. Soc. Symp. Proc. 393 (1995) 151.
[6] P.R. Roberge, Handbook of Corrosion Engineering, McGraw-Hill Companies, Inc., New York, 1999.
[7] N. Perez, Electrochemistry and Corrosion Science, Kluwer Academic Publishers, Boston, 2004.
[8] R. Tian, J. Sun, L. Wang, Int. J. Hydrogen Energy 31 (2006) 1874–1878.
[9] T.L.S.L. Wijesinghe, D.J. Blackwood, Appl. Surf. Sci. 253 (2006) 1006–1009.
[10] A. Fattah-alhosseini, A. Saatchi, M.A. Golozar, K. Raeissi, Electrochim. Acta 54 (2009) 3645–3650.
[11] U.S. Department of Energy, Multi-Year Research, Development and Demonstration Plan: Planned Program Activities for 2005–2015, 2007, http://www1.eere.energy.gov/hydrogenandfuelcells/mypp/pdfs/fuel_cells.pdf, p. 3.4-26.
[12] N.E. Hakiki, M.F. Montemor, M.G.S. Ferreira, M. da Cunha Belo, Corros. Sci. 42 (2000) 687–702.

[13] L.M. Peter, H. Tributsch, Experimental techniques in photoelectrochemistry, in: M.D. Archer, A.J. Nozik (Eds.), Nanostructured and Photoelectrochemical Systems for Solar Photon Convertion, Imperial College Press, London, 2008.
[14] A.M.P. Simões, M.G.S. Ferreira, B. Rondot, M.d.C. Belo, J. Electrochem. Soc. 137 (1990) 82–87.
[15] R. De Gryse, W.P. Gomes, F. Cardon, J. Vennik, J. Electrochem. Soc. 122 (1975) 711–712.
[16] M.F. Montemor, M.G.S. Ferreira, N.E. Hakiki, M.D. Belo, Corros. Sci. 42 (2000) 1635–1650.
[17] H. Tsuchiya, S. Fujimoto, O. Chihara, T. Shibata, Electrochim. Acta 47 (2002) 4357–4366.
[18] M.G.S. Ferreira, M.D.C. Belo, N.E. Hakiki, G. Goodlet, M.F. Montemor, A.M.P. Simões, J. Braz. Chem. Soc. 13 (2002) 433–440.
[19] W.W. Gartner, Phys. Rev. 116 (1959) 84.
[20] S. Fujimoto, H. Tsuchiya, Corros. Sci. 49 (2007) 195–202.
[21] M.J. Carmezim, A.M. Simões, M.O. Figueiredo, M. Da Cunha Belo, Corros. Sci. 44 (2002) 451–465.